RSC Advances

COMMUNICATION

View Article Online
View Journal | View Issue

Cite this: *RSC Adv.*, 2015, **5**, 42798

Received 25th March 2015
Accepted 6th May 2015

DOI: 10.1039/c5ra05298j

www.rsc.org/advances

Nanocasting a mesoporous palladium replica from a body-centered cubic mesoporous silica and palladium and silver metallic nanoarchitectures within mesoporous channels†

Jheng-Guang Li, Cheng-Ying Tsai and Shiao-Wei Kuo*

In this study we employed a facile impregnation method—based on the application of capillary forces, evaporation of solvent and subsequent thermal reduction under H_2—for the synthesis of various metal/mesoporous silica composites. Using this approach we obtained highly dispersed Ag nanoparticles within BCC (body-centered cubic) mesoporous silica, interconnected Pd networks within the BCC mesoporous silica, and Ag and Pd nanowires within hexagonal cylindrical channels, all of which we characterized using small-angle X-ray scattering, transmission electron microscopy, N_2 sorption isotherms, and powder X-ray diffraction. Notably, this paper reports the first example of such a Pd metal replica structure prepared through use of the unique BCC-type mesoporous silica as a hard template and subsequent etching in $HF_{(aq)}$. Finally, we report the successful fabrication of a highly disperse Ag/silica complex prepared through a convenient one-step synthesis.

Introduction

Metal nanostructures, including nanoparticles and nanowires,[1–16] are receiving much attention for their unique properties and wide-ranging potential applications in, for example, catalysis,[17–23] electronics,[24–27] hydrogen storage,[28–31] and magnetics.[32–34] Nanostructured metals present large specific surface areas, making them quite effective nanocatalysts for enhancing chemical reactions on their surfaces—most notably for Pd and Ag nanostructures.[21–23] Therefore, the ability to simultaneously enhance the reaction activity and increase the number of catalysis cycles is a very important issue for both industrial applications and fundamental studies. Although Pd/mesoporous silicas,[35–40] and Ag/mesoporous silicas[41–44] have been used broadly in various heterogeneous catalysis processes, the pore sizes of most mesoporous silicas have been limited to less than 10 nm because of the limited dimensions of the structure directing agent; for example, the well-established template cetyltrimethylammonium bromide (CTAB) produces mesoporous silicas having mesopore dimensions of approximately 3 nm,[45,46] while the commercial template $EO_{20}PO_{70}EO_{20}$ (p123) provides mesopores of approximately 5 nm.[47,48] Recently, we developed a new series of mesoporous silicas having large and tunable mesopores, templated by the lab-made block copolymer poly(ethylene oxide-*b*-caprolactone) (PEO-*b*-PCL) with mesopore sizes increased to the range between 10 and 40 nm.[49,50] In this study, we designed two new large-pore mesoporous silicas with specific mesostructures as matrices for the loading of metallic nanoparticles—namely, mesoporous silicas with body-centered cubic (BCC) and hexagonal cylinder structures, respectively.

In addition to the metallic nanoparticles/porous matrix complex materials mentioned above, pure metallic nanoparticles with specific porous structures are also attractive materials in various fields; one of the most efficient methods for preparing metallic nanoparticles with specific structures is template synthesis.[51] For example, mesoporous silicas with many kinds of mesostructures have been used as hard templates for impregnation with metal precursors in their nanochannels; subsequent reduction of the metal precursors and removal of the silica template can provide metal replicas, including inverse hexagonal cylinders[52,53] and bicontinuous gyroid structures.[54,55] In this study, we took two kinds of mesoporous silicas (one with a BCC structure, the other with an hexagonal cylinder structure) as hard matrices for metal precursors [$AgNO_3$, $Pd(NO_3)_2$] using an incipient wetness impregnation strategy; this approach allowed us to fabricate several distinct structures: interconnected spherical Pd replicas, Pd/cylindrical silica, Ag/BCC silica, and Ag/cylindrical silica.

Through a simple impregnation method, Ag and Pd nanowires are readily prepared in the cylindrical channels of mesoporous silicas; in the critical procedure, after evaporation of the solvent, reduction with H_2 is performed to produce pure metal in the pores. The thermally treated step is the key process to

Department of Materials and Optoelectronic Science, National Sun Yat-Sen University, Kaohsiung, 804, Taiwan. E-mail: kuosw@faculty.nsysu.edu.tw

† Electronic supplementary information (ESI) available. See DOI: 10.1039/c5ra05298j

ensure successful formation of these metal nanowires; as the temperature increases, the metal precursors undergo reduction and then the newly formed metal nanoparticles connect together to form pure nanowires in the channels. Accordingly, control over the temperature is required to obtain the best conditions for fabrication of these metal nanowires. In this study, we synthesized three amphiphilic block copolymers ($EO_{45}CL_{36}$, $EO_{114}CL_{42}$, $EO_{114}CL_{84}$) having different molecular weight as soft templates for the fabrication of a series of mesoporous silicas. The $EO_{114}CL_{42}$-templated silica exhibited a disordered spherical structure as a result of the large volume fraction of the PEO domain; addition of a structure modifier PEO-POSS (star PEO octa-functionalized polyhedral oligomeric silsesquioxane) during the preparation process provided a clear BCC mesophase. The mesoporous silica templated by $EO_{45}CL_{36}$ possessed an apparent hexagonal cylinder structure. When we took these two specific hard templates (BCC and cylinder structures, respectively) to prepare metal/silica complexes through nanocasting, we obtained Pd/BCC and Ag/cylinder silicas exhibiting connected (or aggregated) metallic nanoparticles within their channels. In other words, the Pd/cylinder and Ag/BCC silica complexes displayed more dispersive distributions within the nanopores. Furthermore, to observe how the heating procedure affected the distribution of nano-Pd within the channels, we performed experiments in which we regulated the thermally treated conditions under a H_2 atmosphere. In general, the spherical mesopores of the BCC silicas were interconnected by undetectable, narrow micropores, making it very hard to fill the spherical pores with metallic nanoparticles. Nevertheless, we could successfully fabricate Pd/BCC silica complexes, proving that there were indeed micropores connecting the spherical mesopores; after removal of the silica, however, formed weakly connected Pd linkages that resulted in shrinkage of the ordered BCC mesostructure replicas. In addition, we also successfully employed a one-pot synthesis method to fabricate Ag/silica complexes. We used transmission electron microscopy (TEM), small-angle X-ray scattering (SAXS), N_2 adsorption/desorption isotherms, electron diffraction, and power X-ray diffraction (XRD) spectra to characterize all of these mesoporous silica, metal/silica, and metal replica samples.

Experimental

Materials

Monomethoxy-poly(ethylene glycol)s having molecular weights of 5000 (PEO_{114}) and 2000 (PEO_{45}) were obtained from Fluka. ε-Caprolactone (ε-CL, Acros) was purified through vacuum distillation over CaH_2. Stannous(II) octoate [$Sn(Oct)_2$, Sigma] was used as received. Star PEO-POSS was purchased from Hybrid Plastics (USA); the molecular weight of PEO-POSS was 5576 g mol^{-1}. Silver nitrate ($AgNO_3$) and palladium(II) nitrate dehydrate were taken as metal precursors (Aldrich). Tetraethyl orthosilicate (TEOS) (99%) and hydrochloric acid were obtained from SHOWA (Japan). EtOH (95%) and tetrahydrofuran (THF, >99%) were purchased form ECHO (Taiwan). Diblock copolymers were readily prepared through the ring-opening polymerization (ROP) of ε-CL in the presence of PEO_{114} and $Sn(Oct)_2$. The reaction mixtures were prepared by introducing a desired volume of ε-CL (ε-caprolactone, Acros) monomer into a silanized flask containing a pre-weighed amount of PEO_{114} under a N_2 atmosphere. Several drops of $Sn(Oct)_2$ were added and then the flask was connected to a vacuum line, evacuated, sealed off, and heated at 130 °C. After 24 h, the resulting block copolymers were dissolved in CH_2Cl_2 and precipitated in an excess of cold *n*-hexane. The polymers were dried at 40 °C under vacuum. The characteristics of the diblock copolymers used in this study are summarized in Table 1.

Table 1 Characterization data of PEO-PCL diblock copolymers used in this study

Sample	Abbreviation	NMR M_n[a]	PDI[b]
$EO_{45}CL_{36}$	EC1	6104	1.35
$EO_{114}CL_{42}$	EC2	9788	1.14
$EO_{114}CL_{84}$	EC3	14 576	1.20

[a] Calculated from ^1H NMR spectra. [b] Calculated from gel permeation chromatography (GPC) trace (eluent: DMF; flow rate: 0.4 mL min^{-1}; calibration: polystyrene standards).

Mesoporous silicas templated by PEO-PCL copolymers

Mesoporous silicas were prepared through an evaporation induced self-assembly (EISA) strategy in THF, using various PEO-PCL copolymers ($EO_{45}CL_{36}$, $EO_{114}CL_{42}$, $EO_{114}CL_{84}$; Table 1) as templates and TEOS as the silica precursor (Scheme 1). In a typical synthesis, a TEOS-to-$EO_{114}CL_{42}$ weight ratio of 3 : 1 (for disordered mesoporous silica), a TEOS-to-$EO_{114}CL_{42}$-to-PEO-POSS weight ratio of 3 : 1 : 0.7 (for ordered BCC type mesoporous silica), or a TEOS-to-$EO_{45}CL_{36}$ weight ratio of 1.45 : 1 was used at a constant concentration of HCl (0.012 g of 0.1 M HCl/PEO-PCL); the mixture of TEOS and HCl at a specific composition was added to a stirred solution of PEO-PCL (2.0 wt%, containing 0.10 g of copolymer) in THF (5 g); stirring was continued for 30 min to form a homogeneous solution. The sample was poured into a Petri dish and then the THF was evaporated at room temperature for 48 h. The transparent film was collected, ground into a powder, transferred to a PFA bottle containing 1.0 M HCl (30 mL), and treated hydrothermally at 100 °C for 3 days. The product was washed sequentially with water and EtOH, dried at room temperature, and calcined in air at 600 °C for 6 h to produce a white mesoporous silica. Thermally treated processes were conducted in a furnace operated at a heating rate of 1 °C min^{-1}.

Metal/mesoporous silica composites and Pd replicas

To prepare metallic nanoparticles within its nanoscale channels, a mesoporous silica powder having a specific structure (20 mg) was soaked in a tiny amount of saturated metal precursor solution (*ca.* 13 mg of metal precursor in a suitable amount of water). The product was filtered off, rinsed with a little EtOH, and subjected to thermal treatment to decompose the impregnated metal precursor and form the metal

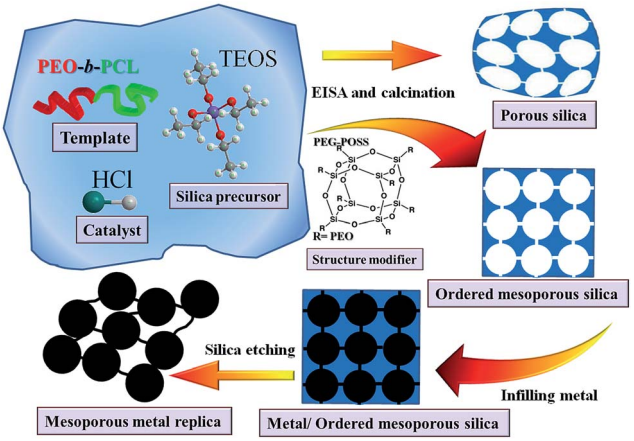

Scheme 1 Preparation of mesoporous silica, ordered mesoporous silica, metal/mesoporous silica, and metal replica samples.

nanostructures (reduction conditions for Ag: 250 °C for 1 h, heating at a rate of 1 °C min^{-1} to 350 °C, and then maintaining that temperature for 2 h; for Pd: 75 °C for 0, 2 or 4 h, heating at 1 °C min^{-1} to 200 °C, and then maintaining that temperature for 2 h; atmosphere: 10% H_2 and 90% N_2). For the Pd/silica complex, removal of the silica in HF solution (10 wt%) provided a Pd replica that possessed mesopores as the final product. In addition, Ag/mesoporous silica composites were prepared through one-pot synthesis: TEOS (0.1 g), $EO_{114}CL_{84}$ (0.1 g), $AgNO_3$ (0.1 g), 0.1 M HNO_3 (0.1 g), and THF (5 g) were stirred to form a homogeneous solution; after slow evaporation of the solvent, thermal reduction was performed directly on the powdered mixture (*i.e.*, the product was formed without hydrothermal treatment).

Characterization

^1H NMR spectra were recorded at room temperature using a Bruker AM 500 (Bruker Corporation, 500 MHz) spectrometer, with the residual proton resonance of the deuterated solvent acting as the internal standard. Molecular weights were determined through gel permeation chromatography (GPC) using a Waters 510 high-performance liquid chromatograph equipped with a 410 differential refractometer and three Ultrastyragel columns (100, 500, and 10^3 Å) connected in series (JASCO Germany GmbH), with dimethylformamide (DMF) as the eluent (flow rate: 0.4 mL min^{-1}). SAXS was performed using a NANOSTAR U small-angle X-ray scattering system (Bruker AXS, Karlsruhe, Germany) and Cu Kα radiation (30 W, 50 kV, 600 μA). The *d*-spacings were calculated using the formula $d = 2\pi/q$, where q is the scattering vector. TEM images were recorded using a JEOL 3010 microscope (JEOL Ltd) operated at 200 kV; samples for TEM measurement were suspended in EtOH and supported onto a holey carbon film on a Cu grid. Nitrogen adsorption/desorption isotherms were measured at −196 °C using an ASAP 2020 analyzer (Micromeritics Instrument Corporation); prior to measurements, the samples were degassed under vacuum at 200 °C for at least 6 h. The Brunauer–Emmett–Teller (BET) method was used to calculate the specific surface areas and pore volumes; pore size distributions were derived from the adsorption branches of the isotherms by using the Barrett–Joyner–Halenda (BJH) model. XRD patterns were recorded using a German Bruker AXS D8 ADVANCE X-ray diffractometer and Cu Kα radiation (λ = 1.541 Å); the products were recorded in the 2θ range from 30 to 90°.

Results and discussion

Metallic nanoparticles within nanochannels of BCC-type mesoporous silica; Pd replica

First, we used the amphiphilic block copolymer $EO_{114}CL_{42}$ (prepared through ROP; PDI = 1.14; M_n = 9788; Table 1) as a template for the preparation of mesoporous silicas having spherical mesopores, as a result of the larger volume fraction of the hydrophilic part (PEO segment) of this PEO-PCL; the random packing of the spherical micelles, however, was not ideal for subsequent nanocasting. Therefore, we introduced a structure modifier, PEO-POSS, to enhance the spherical packing and allowing us to obtain a clear BCC-type mesoporous silica.[50] Next, we employed the BCC mesoporous silica as a hard template for the further impregnation of metallic nanoparticles; in a typical procedure (Scheme 1), the precursor solutions were brought into the mesochannels of the mesoporous silica through an incipient wetness impregnation strategy, taking advantage of capillarity effects. After evaporation of the solvent, the metal precursors were retained within the mesochannels; metallic nanoparticles/silica complexes were eventually formed through thermal reduction under H_2. Fig. 1 displays the three steps leading to the formation of Pd/BCC silica: from disordered spherical mesoporous silica to BCC mesoporous silica and, finally, to Pd/BCC silica. As revealed in Fig. 1a, the primary SAXS peak of the mesoporous silica templated by $EO_{114}CL_{42}$ was strong, but the higher-order scattering peaks were weak, broad,

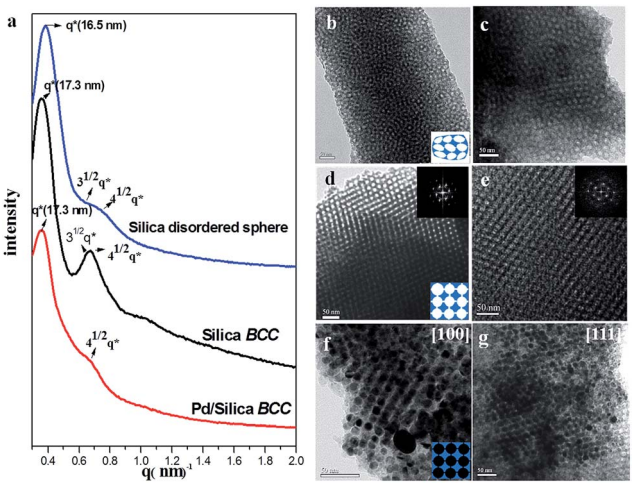

Fig. 1 (a) SAXS patterns of the disordered spherical mesoporous silica templated by $EO_{114}CL_{42}$, the ordered BCC-type mesoporous silica after blending with PEO-POSS during the EISA process, and the Pd/BCC silica nanocomposite. (b–g) TEM images of (b and c) the disordered spherical mesoporous silica, (d and e) the ordered BCC-type mesoporous silica, and (f and g) the Pd/BCC silica nanocomposite.

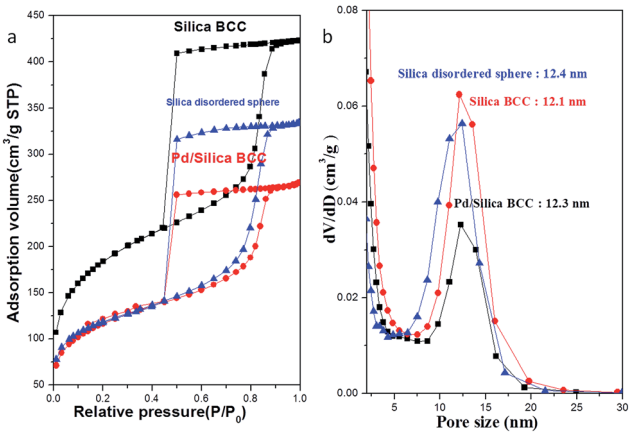

Fig. 2 (a) N_2 adsorption/desorption isotherms and (b) pore size distribution curves of the disordered spherical mesoporous silica, the ordered BCC-type mesoporous silica, and the Pd/BCC silica nanocomposite.

and difficult to recognize, suggesting a poor arrangement of spherical micelles and a lack of long-range ordering. After introducing the structure modifier PEO-POSS into the self-assembly process, the SAXS pattern of the resulting mesoporous silica demonstrated an apparent second-order reflection (Fig. 1a), indicating spherical packing with better ordering; in other words, it revealed the BCC mesophase. However, the scattering ratio of $\sqrt{2q^*}$ and $\sqrt{3q^*}$ since the order of reflection for BCC is SQRT 1, 2, 3, 4. The typical X-ray scattering ratio should be SQRT 1, 2, 3, 4, as shown in revised Fig. 1a, here the peaks of SQRT 3 and 4 are difficult to assign the exact position due the mixed peaks resulted in one broad peak, for the missing reflection of $\sqrt{2q^*}$; we believe that it is the result of intensity combination of form factor and structure factor, it is no doubt the primary peak (q*, (110)) usually display strong reflection, and the form factor of spherical pores packing contributed strong intensity among the reflective ratio of SQRT 3 and 4, (211) and (220), respectively. However, the form factor represented minima intensity at around $\sqrt{2q^*}$ and the original intensity of (200) also exhibited weak intensity, causing the missing of peak $\sqrt{2q^*}$. We observed a low-quality SAXS pattern after the formation of the Pd nano-network within the spherically interconnected mesopores (Fig. 1a). TEM images (Fig. 1b–g) provided evidence consistent with the SAXS characterization data. The mesoporous silica templated by $EO_{114}CL_{42}$ featured a random distribution of spherical mesopores (Fig. 1b and c), similar to a distorted sphere structure. Fig. 1d and e present TEM images of a typical BCC mesophase as viewed from the [100] and [111] planes, respectively; a BCC structure had clearly formed after adding PEO-POSS as a structure modifier. After impregnation and reduction of the Pd precursor, a clear BCC Pd/silica complex appeared; Fig. 1f and g reveal a three-dimensional (3D) array of interconnected Pd nanoparticles, as viewed from the [100] and [111] directions, respectively; in comparison, Fig. 1d and e reveal a square arrangement (Fig. 1f) and hexagonal packing (Fig. 1g) of the Pd nanostructure within the mesopores of the BCC structure. Fig. 2 displays the results of N_2 sorption experiments; we observe that samples 1–3 (disordered spheres, BCC structure, and Pd/BCC structure, respectively; Table 2) provided type-IV isotherms in their N_2 adsorption/desorption curves and exhibited the H_2 hysteresis loops expected for cage-like mesopores (Fig. 2a), consistent with the spherical mesopores of these three samples. We calculated the pore size distributions of the mesoporous silica samples from the adsorption branches of their BET isotherms, based on the BdB sphere model for spherical mesopores (Fig. 2b).[56,57] The pore sizes in all of the mesoporous silica samples ranged approximately from 12.2 to 12.4 nm. In addition, the BET surface area, the micropore surface area, the pore volume, and the micropore volume all decreased after infilling of the Pd metallic nanoparticles (*cf.* samples 2 and 3), but exhibited different trends upon varying the PEO-POSS content. Table 2 lists the primary *d*-spacings, pore sizes, pore volumes, and pore surface areas.

Fig. 3b displays electron diffraction patterns of the TEM image in Fig. 3a; the diffraction rings, with decreasing *d*-spacings, could be indexed to the reflections of the (111), (200), (220), (311) and (222) planes, respectively. The results have two implications: (i) the Pd precursors were indeed reduced after H_2 thermal treatment and (ii) the growth of polycrystalline Pd nanostructures. Fig. 3c, an enlarged image of Fig. 3a, clearly displays the rectangular array of the Pd nanoparticles. Similar to the electron diffraction data, the wide-angle powder X-ray diffraction pattern features five diffraction peaks in the 2θ

Table 2 Textural properties of mesoporous silica and metal/mesoporous silica samples

Sample	d^a (nm)	Pore size (nm)	$S_{BET}{}^b$ ($m^2\ g^{-1}$)	$S_M{}^b$ ($m^2\ g^{-1}$)	Pore volume ($cm^3\ g^{-1}$)	Micropore volume ($cm^3\ g^{-1}$)	Note
1	16.5	12.4	416	148	0.52	0.066	Sphere mesoporous silica
2	17.3	12.2	832	197	0.74	0.083	BCC mesoporous silica
3	17.3	12.2	414	97	0.42	0.041	Pd/BCC mesoporous silica
4	17.3	12.3	452	121	0.40	0.051	Ag/BCC mesoporous silica
5	19.5	19.3	694	176	1.46	0.076	Cylinder mesoporous silica
6	19.5	19.2	511	117	1.01	0.049	Ag/cylinder mesoporous silica
7	19.5	19.4	489	139	1.05	0.060	Pd/cylinder mesoporous silica

[a] The *d*-spacing values were calculated by the formula $d = 2\pi/q^*$. [b] S_{BET} and S_M are the total BET surface area and micropore surface area calculated from the *t*-plots, respectively.

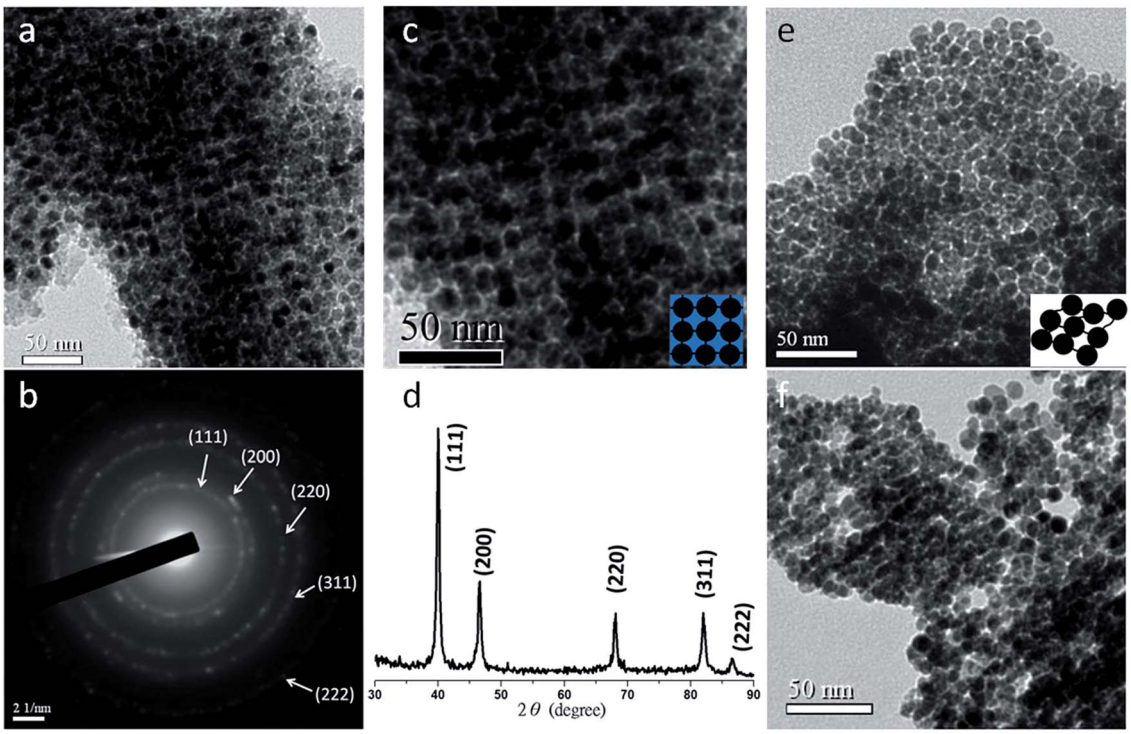

Fig. 3 (a) TEM image, (b) selected-area electron diffraction pattern, (c) enlarged TEM image, and (d) powder XRD pattern of the Pd/BCC mesoporous silica. (e and f) TEM images of the Pd replica.

range from 30 to 90°, representing the (111), (200), (220), (311), and (222) planes of metallic Pd, respectively. We removed the silica hard template to produce a pure Pd replica through etching with $HF_{(aq)}$ as the final step of the template-directed synthesis. The TEM images of pure Pd nanostructures in Fig. 3e and f reveal a Pd nanoparticle array with 3D interconnected links; the narrow Pd links were, however, too weak to support the whole construction, resulting in the Pd replica collapsing to form a spherical stacking structure with poor ordering after removal of the silica. Fig. S1† showed the histogram of Pd metallic nanoparticles with particle size distribution and mean diameter, the mean particle size is 8.6 nm and the particle size was distributed mainly between 6 and 10 nm. Both evidences are corresponded to the pore size distribution reasonably since the metallic particle size should be smaller than the pore size (approximately 12.1 nm). Although hard templates with various structures have been used previously in template-directed synthesis, including face-centered cubic (FCC), hexagonal cylindrical, and bicontinuous gyroid structures, this paper reports, to the best of our knowledge, the first example of the complete fabrication of a BCC metallic nanoparticles network within the large pores of a BCC mesoporous silicas. We anticipate that the unique properties of 3D Pd networks with large cage-like mesopores might have interesting applications, for example as selective catalysts based on a stereohindrance effect.

We used $AgNO_3$ as precursor for the fabrication of Ag/BCC silica composites through incipient wetness impregnation; interestingly, the Ag/BCC silicas exhibited experimental properties distinct from those of the Pd/BCC silicas. As revealed in Fig. 4a and b, Ag nanoparticles were spread throughout the BCC mesoporous silica matrices, implying that the Ag precursor had difficulty moving during the thermal reduction procedure; in other words, it tended to undergo local reduction. Fig. 4c and d display electron diffraction and X-ray diffraction patterns,

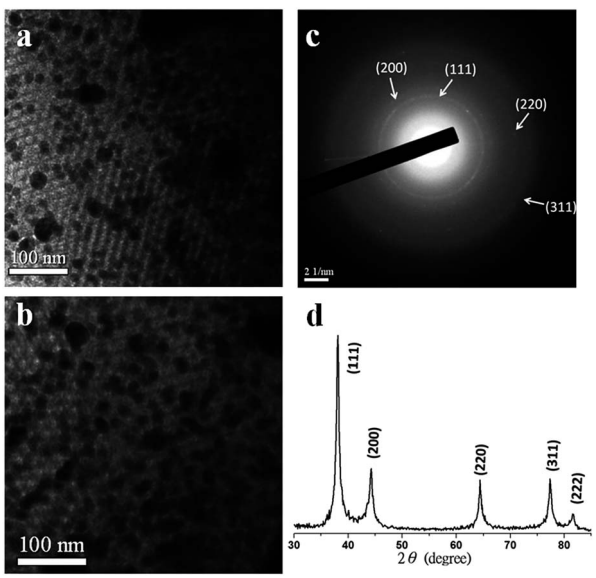

Fig. 4 (a and b) TEM images, (c) selected-area electron diffraction pattern, and (d) powder XRD pattern of the Ag/BCC mesoporous silica.

respectively, of the Ag/BCC silica composite; the decreasing sequence of *d*-spacings could be indexed to the (111), (200), (220), (311), and (222) planes, respectively, suggesting complete reduction of the Ag precursor. Much like the BCC mesoporous silica, the Ag/BCC silica composite also provided a typical type-IV isotherm with a H_2 spherical hysteresis loop (Fig. 5a). We calculated the pore size distribution from the adsorption branch of the sorption curve, based on the BdB model, obtaining a pore size of approximately 12.3 nm, similar to that of hard template BCC mesoporous silica. Table 2 lists the textural properties of sample 4 (Ag/BCC mesoporous silica); thus, a large amount of Ag metallic nanoparticles filled the mesopores, revealing the great dispersibility of the Ag metal particles and suggesting that this composite material might make an excellent heterogeneous catalyst.

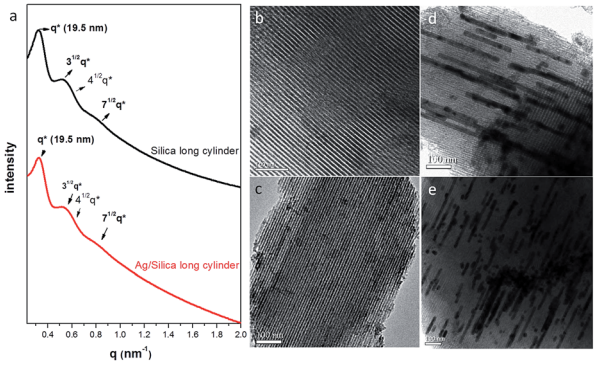

Fig. 6 (a) SAXS patterns of the hexagonal cylinder mesoporous silica and the Ag/cylinder silica. (b–d) TEM images of (b and c) the hexagonal cylinder mesoporous silica and (d and e) the Ag/cylinder silica.

Metallic nanoparticles within mesochannels of hexagonal cylinder mesoporous silica

To template the formation of hexagonal cylindrical mesoporous silicas, we synthesized $EO_{45}CL_{36}$ through ROP, using MPEG-2K (monomethoxy-poly(ethylene glycol) with a molecular weight of 2000) as the macroinitiator. We then prepared Ag/hexagonal silica and Pd/hexagonal silica samples and characterized them in a manner similar to that described above. In Fig. 6a, the SAXS patterns exhibit typical cylinder characteristics, with a $1 : 3^{1/2} : 2 : 7^{1/2}$ reflection ratio, for both the hexagonal cylinder mesoporous silica (sample 5, template $EO_{45}CL_{36}$) and the Ag/cylinder silica composite sample (sample 6). For similar reason, the broad peak was mixed by $3^{1/2}q^*$ and $2q^*$, the scattering vectors have been assigned here. To confirm the structure and the effect of Ag impregnation, Fig. 6b–e display the TEM images of the hard template (Fig. 6b and c, hexagonal cylinder mesoporous silica) and the Ag/cylinder silica (Fig. 6d and e). For the sake of comparison, these TEM images are all similar side views (viewed from the [10] plane). In Fig. 6d and e, the TEM images clearly display Ag nanowires within the cylindrical channels after impregnation and reduction of the Ag precursor. The N_2 sorption isotherms of the two mesoporous silica samples (the samples before and after infilling of Ag (mesoporous silica and Ag/mesoporous silica), respectively) are representative type-IV curves featuring one capillary condensation step (Fig. 7a) and poor H_1-like hysteresis loops, suggesting that the two mesoporous structures (mesoporous silica and Ag/mesoporous silica, respectively) had cylinder-like pores (consistent with the TEM images and SAXS patterns). Fig. 7b reveals that the pore sizes of the two samples are distributed in the approximate range 19.2–19.3 nm, as measured from the adsorption branches based on the Harkins–Jura model.[58] Table 2 lists the textural properties of sample 5 (cylinder mesoporous silica) and sample 6 (Ag/cylinder silica). To obtain more information about the Ag nanowires within the cylindrical channels, Fig. 8b (selected area: TEM image in Fig. 8a and d, selected area: red circle in Fig. 8c) display corresponding electron diffraction patterns. When we analyzed a large area of the Ag/cylinder silica sample, we observed polycrystalline distribution characteristics of Ag metal growth, consistent with the indistinct diffraction rings of the (111), (200), (220), and (311) planes, respectively. An interesting phenomenon appeared when we analyzed a small area of the Ag/cylinder silica samples (indicated by the red circle in Fig. 8c): some degree of orientation of the Ag nanowires

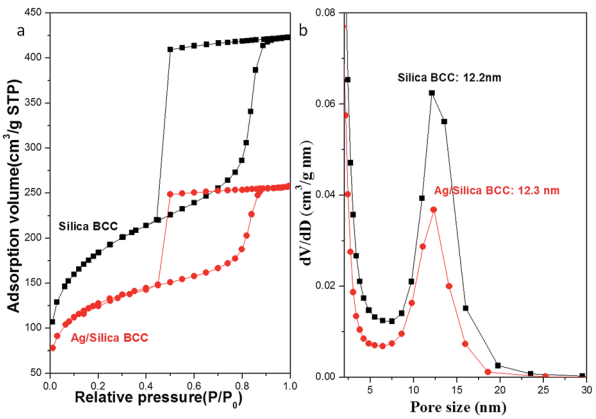

Fig. 5 (a) N_2 adsorption/desorption isotherms and (b) pore size distribution curves of the BCC-type mesoporous silica and the Ag/BCC silica.

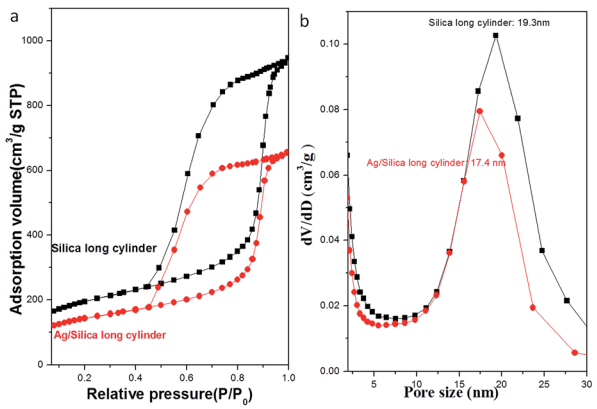

Fig. 7 (a) N_2 adsorption/desorption isotherms and (b) pore size distribution curves of the hexagonal cylinder mesoporous silica and the Ag/cylinder silica.

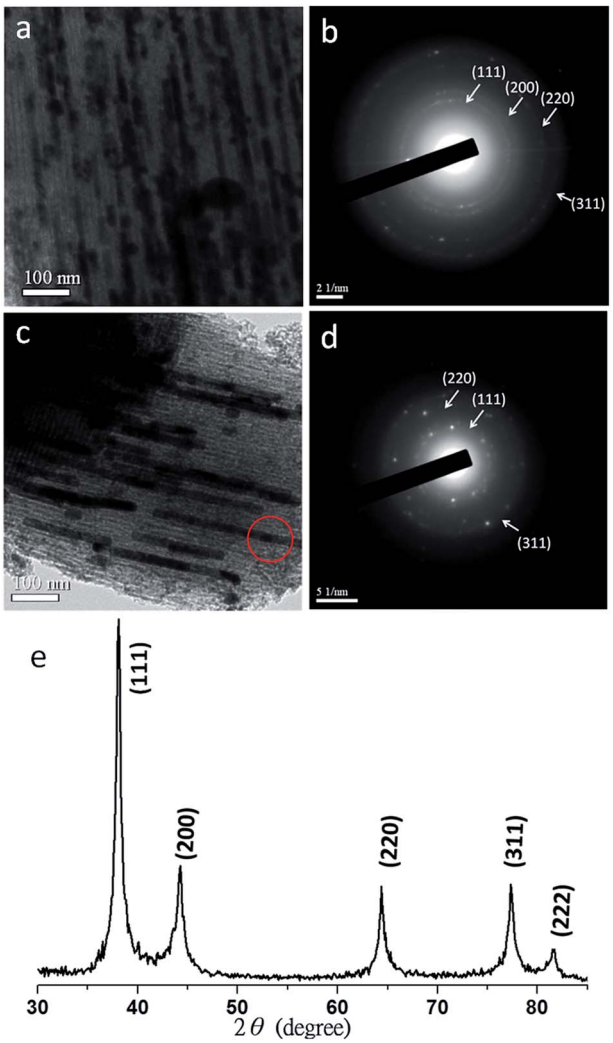

Fig. 8 (a) TEM image and (b) selected-area electron diffraction pattern of (a); (c) TEM image and (d) selected-area electron diffraction pattern of the red circle in (c); and (e) powder XRD pattern of the Ag/cylinder silica.

appeared, suggested by the occurrence of some clear diffraction spots (indicated by the white arrows in Fig. 8d). This observation implies that the Ag nanowire grew from a specific direction during the thermal reduction process. XRD analysis of the Ag/cylinder silica sample revealed the Ag metallic phase, represented by the (111), (200), (220), and (311) reflections, respectively, with increasing values of 2θ (Fig. 8e). According to the description of related article,[13] we know the crystalline orientation mainly resulted from the two key points, one is the interaction between metal precursors and silica walls, and the other is the crystalline temperature.

The morphology of the Pd/cylinder silica underwent an apparent transformation upon changing the thermal reduction conditions under the H_2 atmosphere (Fig. 9b–g). Initially, we increased the thermally treated temperature gradually (heating rate: 1 °C min^{-1}) to a temperature of 200 °C and then maintained the system at this temperature for 2 h at to ensure complete reduction of the Pd precursor. The heating conditions

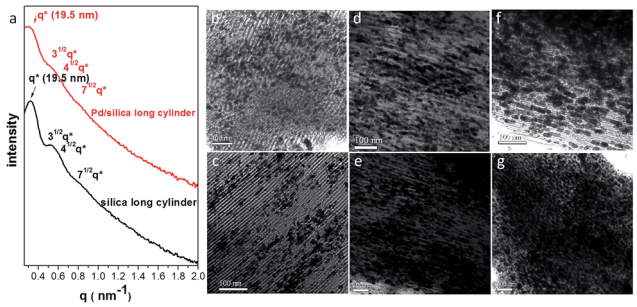

Fig. 9 (a) SAXS patterns of the hexagonal cylinder mesoporous silica and the Pd/cylinder silica; (b–g) TEM images of the Pd/cylinder silica under the thermally treated conditions of (b and c) continuous heating, (d and e) maintaining the system at 75 °C for 2 h, and (f and g) maintaining the system at 75 °C for 4 h.

did, however, greatly affect the morphology of the growing Pd nanowires within the cylindrical mesopores during this thermally treated process. Therefore, we tested three different heating conditions to observe their effects on the morphology of the resulting Pd nanowires: maintaining heating without any postponement (Fig. 9b and c), maintaining at 75 °C for 2 h (Fig. 9d and e), and maintaining at 75 °C for 4 h (Fig. 9f and g). TEM images provided direct evidence for the morphological transformations of these Pd nanostructures within the hexagonal channels. Fig. 9b and c reveal metallic Pd nanoparticles or short rods dispersed within the mesopores (side view of the hexagonal cylinder structure), implying that the rate of reduction was too rapid to ensure that the Pd intermediates could move and connect together under the constant heating conditions. When we maintained the temperature at 75 °C for 4 h during the thermally treated procedure, however, many metal intermediates gathered together to form a disordered stack of Pd particles (Fig. 9f and g); accordingly, these reduction conditions were still not ideal for the preparation of Pd nanostructures. As indicated in Fig. 9a, d, and e, however, the SAXS patterns of the Pd/cylinder silica nanocomposites exhibited a reflection ratio of $1 : \sqrt{3} : \sqrt{7}$ after impregnation of the Pd

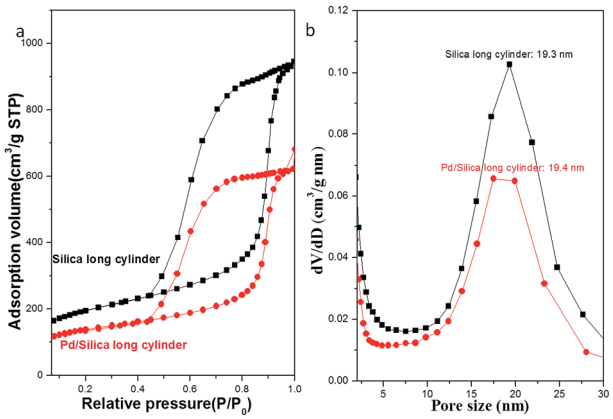

Fig. 10 (a) N_2 adsorption/desorption isotherms and (b) pore size distribution curves of the hexagonal cylinder mesoporous silica and the Pd/cylinder silica.

nanowires under the suitable thermal reduction conditions (heating rate: 1 °C min^{-1}; holding for 2 h at 75 and 200 °C), indicative of an hexagonal cylinder arrangement. In addition, the side-view TEM images in Fig. 9d and e reveal the more-ideal distribution of the hexagonal cylinders. The N_2 sorption isotherms of the sample 7 (Pd/cylinder silica; calcined at 75 and 200 °C for 2 h; heating rate: 1 °C min^{-1}) display (Fig. 10) representative type-IV curves with sharp capillary condensation steps in the relative pressure range from 0.85 to 0.95, suggesting regular mesostructures. Similar to sample 5 (cylinder mesoporous silica), the hysteresis loop exhibited a poor H_1-like shape and a pore size of approximately 19.4 nm, measured based on the Harkins and Jura model. In view of the difference in pore volumes between samples 5 and 7 (Table 2), we calculated an infilling ratio of 28%; Table 2 lists all of the other textual properties of sample 7. To obtain more information, Fig. 11b and c display the electron diffraction and XRD analyses, respectively, of the Pd/cylinder silica composite; typical metallic Pd reflections are indicated as (111), (200), (220), (311) and (222), respectively, suggesting that the Pd precursor had been reduced completely to form the Pd nanostructure in Fig. 11a.

One-pot synthesis of Ag/mesoporous silica nanocomposite

To simplify the fabrication of the metal/mesoporous matrix catalysts, we designed a one-pot synthesis of the Ag/mesoporous silica nanocomposite as the goal product (Fig. 12). Here, we used $EO_{114}CL_{84}$ (Table 1) as the template, TEOS as the silica precursor, $AgNO_3$ as the metallic Ag precursor, and $HNO_{3(aq)}$ as the catalyst for the sol–gel reaction of TEOS. We employed $HNO_{3(aq)}$ as the acid catalyst in place of the original $HCl_{(aq)}$ to avoid the Cl^- ions co-precipitating with the Ag^+ ions and, thereby, not maintaining a dispersed state with the template ($EO_{114}CL_{84}$).

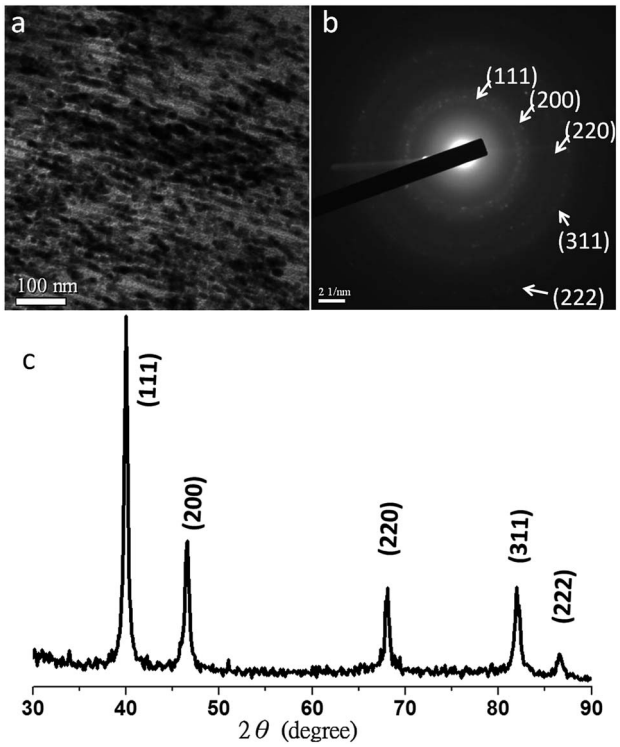

Fig. 11 (a) TEM images, (b) selected-area electron diffraction pattern, and (c) powder XRD pattern of the Ag/cylinder mesoporous silica prepared under thermally treated conditions of maintaining the sample at 75 °C for 2 h.

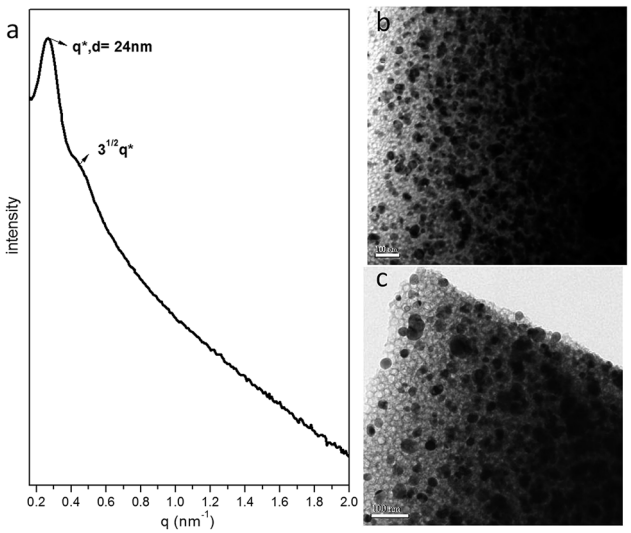

Fig. 12 (a) SAXS pattern and (b and c) TEM images of the Ag/mesoporous silica nanocomposite prepared through one-pot synthesis.

We mixed all of the reagents to form a homogeneous solution; after EISA and thermally treated under H_2, we obtained the Ag/mesoporous silica composite. The SAXS pattern of the nanocomposite (Fig. 12a) reveals a sharp primary signal, implying the regular arrangement of this material; furthermore, TEM images (Fig. 12b and c) provide clear evidence for highly dispersed Ag nanoparticles within the mesopores of the mesoporous silica. The Pd/matrix catalyst already obtained the great achievement in some area, for example, selective catalysis of heck reaction,[59] however, it need multiple experimental steps, such as preparation of supported mesoporous material and further fabrication of heterocatalyst (Pd/C, Pd/silica, *etc.*). If we combine the two procedures into one step, it would be more convenient to prepare such catalyst, in previous study,[60] there is similar experiment to be finished, and they use the common mesoporous MCM-41 as supported materials and involved the Pd precursor into the preparation of MCM-41 in the aqueous system. In our system, however, it would be the new aspect of one-pot preparation of heterocatalyst on the basis of the unusual EISA method. In the future, this could be applied to many different water-insoluble template such as PEO-PCL, PEO-PLA, PEO-PLLA to build various metal/mesoporous material catalyst. Accordingly, we believe that this facile method might be a means of fabricating Ag/porous matrices for use as heterogeneous catalysts.

Conclusions

In this study, we synthesized a series of PEO-PCL diblock copolymers—$EO_{45}CL_{36}$, $EO_{114}CL_{42}$, and $EO_{114}CL_{84}$—with three

different molecular weights for the fabrication of mesoporous silicas through simple ROP. The mesoporous silica featuring a disordered spherical mesostructure, templated by $EO_{114}CL_{42}$, could be transformed into an ordered BCC mesostructure after blending the polymeric template with PEO-POSS as a structure modifier. We then used the BCC mesoporous silica as a matrix to fabricate Pd/silica and Ag/silica complexes. For the Pd/silica sample, we observed the Pd particles packed within the BCC spherical channels, there should be interconnected channels (micropores) among these spherical mesopores; for the Ag/silica sample, we obtained highly disperse Ag nanoparticles within the spherical mesopores. Both materials appear to have future applications in heterogeneous catalysis. Furthermore, Ag or Pd nanowires could also be prepared within the hexagonal cylindrical mesopores of the silica that had been templated by $EO_{45}CL_{36}$. In Ag/cylinder silica sample, some degree of growth and orientation of the Ag nanowires were revealed in TEM images and electron diffraction patterns; for the Pd/cylinder silica sample, we used TEM to investigate the growth of the Pd nanowires during the thermal reduction procedure under H_2. Finally, we developed a convenient one-pot method for the synthesis of a highly disperse Ag/silica complex.

Acknowledgements

This study was supported financially by the National Science Council, Taiwan, Republic of China, under contracts NSC 100-2221-E-110-029-MY3 and NSC-100-2628-E-110-001.

Notes and references

1 E. Choi, M. Kwak, B. Jang and Y. Piao, *Nanoscale*, 2013, **5**, 151–154.
2 Y. Wang, Y. Zhu, J. Chen and Y. Zeng, *Nanoscale*, 2012, **4**, 6025–6031.
3 X. B. Huang, W. J. Dong, G. Wang, M. Yang, L. Tan, Y. H. Feng and X. X. Zhang, *J. Colloid Interface Sci.*, 2011, **359**, 40–46.
4 S. W. Kuo, H. Y. Yang, C. F. Wang and K. U. Jeong, *Macromol. Chem. Phys.*, 2012, **213**, 344–350.
5 A. Takai, Y. Doi, Y. Yamauchi and K. Kuroda, *J. Phys. Chem. C*, 2010, **114**, 7586–7593.
6 A. Fukuoka, H. Araki, J. Kimura, Y. Sakamoto, T. Higuchi, N. Sugimoto, S. Inagaki and M. Ichikawa, *J. Mater. Chem.*, 2004, **14**, 752–756.
7 S. W. Kuo, Y. C. Wu, C. H. Lu and F. C. Chang, *J. Polym. Sci., Part B: Polym. Phys.*, 2009, **47**, 811–819.
8 A. Fukuoka, H. Araki, Y. Sakamoto, S. Inagaki, Y. Fukushima and M. Ichikawa, *Inorg. Chim. Acta*, 2003, **350**, 371–378.
9 K. B. Lee, S. M. Lee and J. Cheon, *Adv. Mater.*, 2001, **13**, 517–520.
10 Y. Zhang, F. L. Y. Lam, X. J. Hu, Z. F. Yan and P. Sheng, *J. Phys. Chem. C*, 2007, **111**, 12536–12541.
11 H. Araki, A. Fukuoka, Y. Sakamoto, S. Inagaki, N. Sugimoto, Y. Fukushima and M. Ichikawa, *J. Mol. Catal. A: Chem.*, 2003, **199**, 95–102.
12 A. Pourahmad and S. Sohrabnezhad, *J. Alloys Compd.*, 2009, **484**, 314–316.
13 H. F. Yang and D. Y. Zhao, *J. Mater. Chem.*, 2005, **15**, 1217–1231.
14 C. M. Yang, H. S. Sheu and K. J. Chao, *Adv. Funct. Mater.*, 2002, **12**, 143–148.
15 H. Y. Fan, K. Yang, D. M. Boye, T. Sigmon, K. J. Malloy, H. F. Xu, G. P. Lopez and C. J. Brinker, *Science*, 2004, **304**, 567–571.
16 R. Ryoo, S. H. Joo, M. Kruk and M. Jaroniec, *Adv. Mater.*, 2001, **13**, 677–681.
17 J. M. Campelo, D. Luna, R. Luque, J. M. Marinas and A. A. Romero, *ChemSusChem*, 2009, **2**, 18–45.
18 S. H. Joo, J. Y. Park, C. K. Tsung, Y. Yamada, P. D. Yang and G. A. Somorjai, *Nat. Mater.*, 2009, **8**, 126–131.
19 N. T. S. Phan, M. Van Der Sluys and C. W. Jones, *Adv. Synth. Catal.*, 2006, **348**, 609–679.
20 J. M. Sun and X. H. Bao, *Chem.–Eur. J.*, 2008, **14**, 7478–7488.
21 I. Yuranov, P. Moeckli, E. Suvorova, P. Buffat, L. Kiwi-Minsker and A. Renken, *J. Mol. Catal. A: Chem.*, 2003, **192**, 239–251.
22 J. D. Webb, S. MacQuarrie, K. McEleney and C. M. Crudden, *J. Catal.*, 2007, **252**, 97–109.
23 J. Han, P. Fang, W. J. Jiang, L. Y. Li and R. Guo, *Langmuir*, 2012, **28**, 4768–4775.
24 A. Fukuoka and M. Ichikawa, *Top. Catal.*, 2006, **40**, 103–109.
25 A. V. Korzhak, N. I. Ermokhina, A. L. Stroyuk, V. K. Bukhtiyarov, A. E. Raevskaya, V. I. Litvin, S. Y. Kuchmiy, V. G. Ilyin and P. A. Manorik, *J. Photochem. Photobiol., A*, 2008, **198**, 126–134.
26 K. Kwon, S. A. Jin, C. Pak, H. Chang, S. H. Joo, H. I. Lee, J. H. Kim and J. M. Kim, *Catal. Today*, 2011, **164**, 186–189.
27 Y. Yamauchi and K. Kuroda, *Chem.–Asian. J.*, 2008, **3**, 664–676.
28 C. Liu, F. Li, L. P. Ma and H. M. Cheng, *Adv. Mater.*, 2010, **22**, E26–E28.
29 D. Saha and S. G. Deng, *Langmuir*, 2009, **25**, 12550–12560.
30 A. M. Seayad and D. M. Antonelli, *Adv. Mater.*, 2004, **16**, 765–777.
31 Z. X. Wu and D. Y. Zhao, *Chem. Commun.*, 2011, **47**, 3332–3338.
32 K. Ariga, A. Vinu, Y. Yamauchi, Q. M. Ji and J. P. Hill, *Bull. Chem. Soc. Jpn.*, 2012, **85**, 1–32.
33 K. S. Napolsky, A. A. Eliseev, A. V. Knotko, A. V. Lukahsin, A. A. Vertegel and Y. D. Tretyakov, *Mater. Sci. Eng., C*, 2003, **23**, 151–154.
34 W. Wang, H. Y. Wang, W. Wei, Z. G. Xiao and Y. Wan, *Chem.–Eur. J.*, 2011, **17**, 13461–13472.
35 S. Banerjee, H. Khatri, V. Balasanthiran, R. T. Koodali and G. Sereda, *Tetrahedron*, 2011, **67**, 5717–5724.
36 Z. Chen, Z. M. Cui, F. Niu, L. Jiang and W. G. Song, *Chem. Commun.*, 2010, **46**, 6524–6526.
37 C. He, F. W. Zhang, L. Yue, X. S. Shang, J. S. Chen and Z. P. Hao, *Appl. Catal., B*, 2012, **111**, 46–57.
38 N. Koizumi, X. Jiang, J. Kugai and C. S. Song, *Catal. Today*, 2012, **194**, 16–24.

39 C. Sotiriou-Leventis, X. J. Wang, S. Mulik, A. Thangavel and N. Leventis, *Synth. Commun.*, 2008, **38**, 2285–2298.
40 Y. Wan, H. Y. Wang, Q. F. Zhao, M. Klingstedt, O. Terasaki and D. Y. Zhao, *J. Am. Chem. Soc.*, 2009, **131**, 4541–4550.
41 E. Qayyum, V. A. Castillo, K. Warrington, M. A. Barakat and J. N. Kuhn, *Catal. Commun.*, 2012, **28**, 128–133.
42 P. Pootawang, N. Saito and O. Takai, *Mater. Lett.*, 2011, **65**, 1037–1040.
43 B. Naik, S. Hazra, V. S. Prasad and N. N. Ghosh, *Catal. Commun.*, 2011, **12**, 1104–1108.
44 H. Zhao, J. C. Zhou, H. Luo, C. Y. Zeng, D. H. Li and Y. J. Liu, *Catal. Lett.*, 2006, **108**, 49–54.
45 J. S. Beck, J. C. Vartuli, W. J. Roth, M. E. Leonowicz, C. T. Kresge, K. D. Schmitt, C. T. W. Chu, D. H. Olson, E. W. Sheppard, S. B. McCullen, J. B. Higgins and J. L. Schlenker, *J. Am. Chem. Soc.*, 1992, **114**, 10834–10843.
46 C. T. Kresge, M. E. Leonowicz, W. J. Roth, J. C. Vartuli and J. S. Beck, *Nature*, 1992, **359**, 710–712.
47 D. Y. Zhao, Q. S. Huo, J. L. Feng, B. F. Chmelka and G. D. Stucky, *J. Am. Chem. Soc.*, 1998, **120**, 6024–6036.
48 D. Y. Zhao, J. L. Feng, Q. S. Huo, N. Melosh, G. H. Fredrickson, B. F. Chmelka and G. D. Stucky, *Science*, 1998, **279**, 548–552.
49 J. G. Li and S. W. Kuo, *RSC Adv.*, 2011, **1**, 1822–1833.
50 J. G. Li, Y. H. Chang, Y. S. Lin and S. W. Kuo, *RSC Adv.*, 2012, **2**, 12973–12982.
51 A. Fukuoka, H. Araki, Y. Sakamoto, N. Sugimoto, H. Tsukada, Y. Kumai, Y. Akimoto and M. Ichikawa, *Nano Lett.*, 2002, **2**, 793–795.
52 Y. J. Han, J. M. Kim and G. D. Stucky, *Chem. Mater.*, 2000, **12**, 2068–2069.
53 C. W. Wu, Y. Yamauchi, T. Ohsuna and K. Kuroda, *J. Mater. Chem.*, 2006, **16**, 3091–3098.
54 H. J. Wang, H. Y. Jeong, M. Imura, L. Wang, L. Radhakrishnan, N. Fujita, T. Castle, O. Terasaki and Y. Yamauchi, *J. Am. Chem. Soc.*, 2011, **133**, 14526–14529.
55 Y. Doi, A. Takai, Y. Sakamoto, O. Terasaki, Y. Yamauchi and K. Kuroda, *Chem. Commun.*, 2010, **46**, 6365–6367.
56 J. C. P. Broekhoff and J. H. deBoer, *J. Catal.*, 1967, **9**, 8–14.
57 M. M. Wan, X. D. Sun, S. Liu, J. Ma and J. H. Zhu, *Microporous Mesoporous Mater.*, 2014, **199**, 40–49.
58 W. D. Harkin and G. Jura, *J. Am. Chem. Soc.*, 1994, **66**, 1366–1377.
59 Y. Wan, H. Wang, Q. Zhao, M. Klingstedt, O. Terasaki and D. Zhao, *J. Am. Chem. Soc.*, 2009, **131**, 4541–4550.
60 C. Sener, T. Dogu and G. Dogu, *Microporous Mesoporous Mater.*, 2006, **94**, 89–98.